PHYSICAL REVIEW E **103**, 063211 (2021)

Collisional excitation kinetics for $O(3s\ ^5S^o)$ and $O(3p\ ^5P_3)$ states using laser absorption spectroscopy in shock-heated weakly ionized O_2-Ar mixture

Yang Li,[*] Yu Wang, David F. Davidson, and Ronald K. Hanson
Department of Mechanical Engineering, Stanford University, Stanford, California 94305, USA

(Received 10 December 2020; accepted 26 May 2021; published 21 June 2021)

Collisional excitation kinetics for atomic oxygen is studied behind reflected shock waves in 1% O_2/Ar mixtures over 10 000–11 000K using laser absorption spectroscopy of the $O(3s\ ^5S^o)$ to $O(3p\ ^5P_3)$ transition at 777 nm and the $O(3p\ ^5P_3)$ to $O(3d\ ^5D^o_{2,3,4})$ transitions at 926 nm. Four time histories are inferred simultaneously from the absorbance of the two transitions: the population density of level 4 of atomic oxygen, i.e., the $O(3s\ ^5S^o)$ state, n_4; the population density of level 6 of atomic oxygen, i.e., the $O(3p\ ^5P_3)$ state, n_6; the electron number density, n_e; and the heavy-particle translational temperature, T_{tr}. Atomic oxygen in the levels 4 and 6 are not in equilibrium with the ground-state atomic oxygen as the measurements of n_4 and n_6 are generally 3–20 times smaller than the corresponding values under Boltzmann equilibrium at T_{tr}. However, these two states are close to partial equilibrium with each other within the test time, indicating strong heavy-particle cross coupling between levels 4 and 6 of atomic oxygen. A simplified two-temperature collisional-radiative (CR) model is developed to study the thermal and chemical nonequilibrium of atomic oxygen following shock heating. The four measured time histories are used to optimize the 12 collisional rate constants in the CR model using a stochastic gradient descent (SGD) algorithm. The time-history results, diagnostic methods, and collisional-radiative model presented in the current study are potentially useful in studies of high-enthalpy air, plasma processing, or other applications involving weakly ionized oxygen.

DOI: 10.1103/PhysRevE.103.063211

I. INTRODUCTION

Under typical atmospheric re-entry conditions of a spacecraft, a bow shock forms ahead of the vehicle because of its high velocity [1–3]. The temperature immediately after the bow shock can be higher than 10 000 K [4,5]. At such high temperatures, molecular oxygen and nitrogen dissociate almost completely and produce atomic species in excited energy states and charged particles [6–8]. Radiation from the excited states can account for a significant portion of the total heat flux to the re-entry vehicle [1,5,9]. This radiation is heavily dependent on the population of the excited-state species, which are generally not in chemical and thermal equilibrium. Understanding the collisional excitation and ionization kinetics for atomic species is thus of crucial importance in predicting the evolution of the population of the excited-state species and thus the radiative heat flux for high-enthalpy air during re-entry missions [7].

In local thermal equilibrium (LTE), the populations of atomic oxygen in various electronic energy states follow the Boltzmann distribution characterized by a single temperature T [10]. Under large spatial or temporal gradients, however, the collisions among particles may not be sufficient to maintain such equilibrium [11]. Some multitemperature kinetic models [9] assume that the excited-state species are in a Boltzmann distribution within each internal mode and therefore are characterized by electron translational temperature T_e, heavy-particle translational temperature T_{tr}, electronic temperature T_{el}, vibrational temperature T_{vib}, and rotational temperature T_{rot}, respectively. More generally, a state-to-state collisional-radiative model can be used to study the kinetic behavior of the excited-state species individually [1,8,12–14]. Most of the previous kinetic models focus on the electron impact collisions because of the higher efficiency of electrons in exciting and ionizing molecules[1,6,7,12]. However, heavy-particle-impact collisional excitation reactions [e.g., $Ar + O(g) = Ar + O(3s\ ^5S^o)$] can be important to the kinetics of high-enthalpy gases [2,8,15,16], especially immediately behind the shock, where electrons are being produced from ionization processes but the number density is still low.

Bultel *et al.* [2], Lemal *et al.* [8], and Jo *et al.* [16] included the heavy-particle excitation rate constants in their state-to-state collisional-radiative models. Nations *et al.* [15] determined the heavy-particle excitation rate of the $O(3s\ ^5S^o)$ state from its population time-history measurements using a 777-nm laser over 5 000–7 000 K. Their measurements showed that the population of the $O(3s\ ^5S^o)$ state remained three to five times smaller than the equilibrium value calculated from the Boltzmann distribution, during their experiment.

Li *et al.* [17] extended the measurements of the $O(3s\ ^5S^o)$ population time-history and the heavy-particle reaction rate to 8 000–10 000 K. These authors observed that the $O(3s\ ^5S^o)$ population time history had three stages within the 1-ms test time after the passage of the reflected shock wave. To explain this behavior, a two-temperature collisional-radiative model was developed, recognizing that electrons are not in thermal

---

[*] yli28@stanford.edu

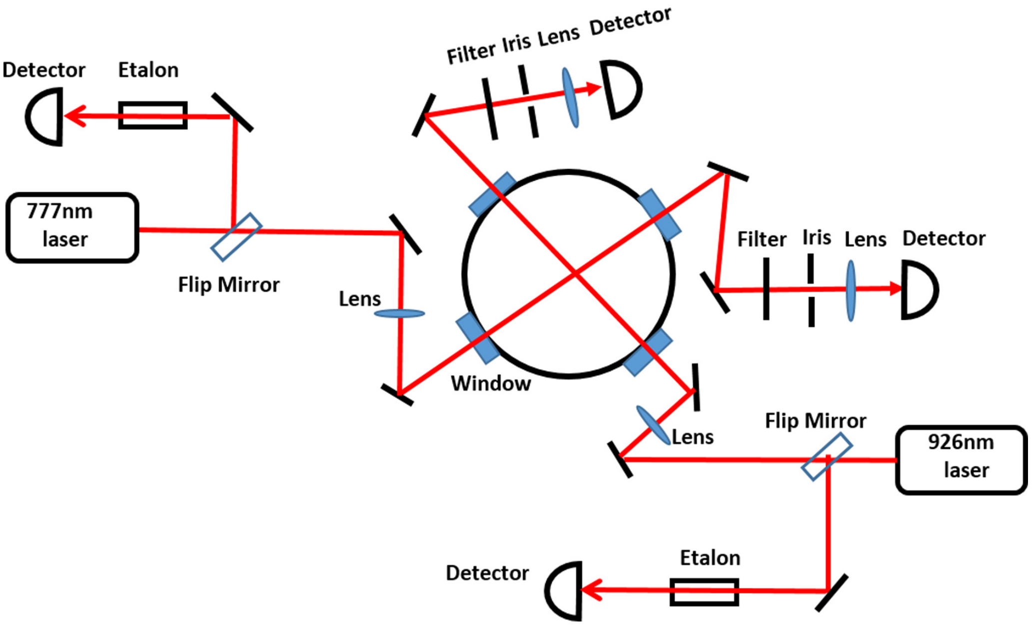

FIG. 1. Optical setup for absorbance measurements of the 777- and 926-nm transitions.

and chemical equilibrium within the test time. This model takes the initial temperature, pressure, and mole fractions after the reflected shock as inputs, solves two energy conservation equations and five species conservation equations, and outputs the time histories of the translational temperature, O(3s $^5S^o$) population, electron number density, and populations of ground-state argon and ground-state atomic oxygen, Ar^+ and O^+. Electron number density and the heavy-particle translational temperature are particularly important to the collisional excitation kinetics of atomic oxygen because of the higher excitation efficiency of electrons compared with heavy particles and the exponential dependence of the excitation rate constants on the translational temperature. Direct measurements of the electron number density and the translational temperature are thus needed to validate and improve the kinetic model.

To improve and extend the previous two-temperature collisional-radiative model for atomic oxygen [17], four time histories, i.e., for the O(3s $^5S^o$) population n_4, the O(3p $^5P_3$) population n_6, the electron number density n_e, and the translational temperature T_{tr}, are simultaneously inferred using two lasers at 777 and 926 nm targeting the O(3s $^5S^o$) to O(3p $^5P_3$) and the O(3p $^5P_3$) to O(3d $^5D^o_{2,3,4}$) transitions from 10 000 to 11 000 K in the current study. The reaction rate constants of the kinetic model are optimized by minimizing the residual sum of squares between the model outputs and the measured time histories.

The goals of this study are (1) to extend the diagnostic methods for atomic oxygen to include the n_4, n_6, n_e, and T_{tr} time histories and to extend the measurement temperature range to 10 000–11 000K, (2) to study the thermal and chemical nonequilibrium behavior of the excited states of atomic oxygen over 10 000–11 000K, and (3) to utilize the measured time histories to optimize the rate constants of the two-temperature collisional-radiative model for Ar-O_2 mixtures over 10 000–11 000 K.

II. EXPERIMENTAL RESULTS

A. Experimental setup

The schematic of the current experiment is presented in a previous paper [18] and repeated here in Fig. 1. The shock tube and laser absorption spectroscopy probing the O(3s $^5S^o$) to O(3p $^5P_3$) transition are described in detail in previous papers [17,18] and summarized below.

In a typical shock tube experiment in this study, the driven section of the shock tube was filled with 1% O_2/Ar (Praxair) to 0.7–1 torr. Then the driver section was filled with He (Praxair) to approximately 130–160 psia until the diaphragm separating the equal-area driver and driven sections ruptured. An incident shock was formed and traveled down the driven section. It was reflected off the end wall, and the stagnant gas behind the reflected shock was heated to initial temperatures over 10 000 K. The velocity of the incident shock was measured using five piezoelectric pressure transducers and extrapolated to infer the velocity at the end wall. The temperature and pressure immediately behind the reflected shock were calculated using an in-house code named frozen-chemistry shock calculator (FROSH), under the assumptions of no oxygen dissociation but vibrational and rotational equilibrium. The typical initial postshock thermodynamic condition was 10 100–11 200 K and 0.3–0.5 atm. The typical duration of approximately constant pressure, i.e., the test time, was 500–600 μs, which was terminated by arrival of the reflection of the reflected shock from the contact surface of the driver and driven gas. The light beam of a 777.2-nm laser Nanoplus targeting the O(3s $^5S^o$) to O(3p $^5P_3$) transition was propagated through a pair of wedged UV-fused silica windows located 5 mm from the end wall. The light beam of a 926-nm laser Nanoplus, targeting the O(3p $^5P_3$) to O($^5D^0_{2,3,4}$) transition was propagated through another pair of wedged UV-fused silica windows at the same axial location. Both of the lasers were modulated by 25-kHz triangle waves. Etalons with free

TABLE I. Spectroscopic parameters for atomic oxygen transitions. E_l and E_u are the energy in wave number of the lower and upper states l and u. A_{ul} is the Einstein coefficient of the transition from u and l. g_l and g_u are the degeneracies of the l and u states.

Transition	Ritz wavelength in air (nm)	A_{ul} (s^{-1})	E_l (cm^{-1})	E_u (cm^{-1})	g_l	g_u
$3s\,^5S$–$3p\,^5P_3$	777.194	3.69×10^7	73768.200	86631.454	5	7
$3p\,^5P_3$–$3d\,^5D_2$	926.5826	2.97×10^6	86631.454	97420.839	7	5
$3p\,^5P_3$–$3d\,^5D_3$	926.5932	1.48×10^7	86631.454	97420.716	7	7
$3p\,^5P_3$–$3d\,^5D_4$	926.6006	4.45×10^7	86631.454	97420.630	7	9

spectral range (FSR) of 0.0688 cm^{-1} were used to convert the laser light from the time domain to the frequency domain. The transmitted light intensities were measured by photodiode detectors (Thorlabs PDA36A, $f_{-3\,\mathrm{dB}} \geqslant 1.6\,\mathrm{MHz}$) and recorded at a sampling rate of 100 MS/s.

B. Spectroscopic theory

The absorbance α_ν at laser frequency ν is determined from the incident and transmitted light intensities by

$$\alpha_\nu = -\ln\left(\frac{I_t}{I_0}\right) = S_{lu} n_l L \phi(\nu), \tag{1}$$

where I_t and I_0 are the transmitted and incident light intensity, respectively; n_l is the number density of atomic oxygen in the the probed state $O(3s\,^5S^o)$ or $O(3p\,^5P_3)$; $L = 15.24$ cm is the optical path length; $\phi(\nu)$ is the line-shape function of the absorbance, which satisfies $\int_0^\infty \phi(\nu)d\nu = 1$ and ν is in cm^{-1}; S_{lu} is the line strength of the transition and is given by

$$S_{lu}[\mathrm{cm/molec}] = \frac{c}{8\pi\nu_0^2} A_{ul} \frac{g_u}{g_l}\left[1 - \exp\left(-\frac{h\nu_0}{k_B T}\right)\right], \tag{2}$$

where c is speed of light in cm/s, ν_0 is the transition frequency in Hz, A_{ul} is the Einstein coefficient of the transition in s^{-1}, and g_u and g_l are the degeneracies of the upper and lower states as summarized in Table I. Because the line strength (S_{lu}) is only weakly dependent on temperature (T), the translational temperature inferred before O_2 dissociation is used in the above equation for simplicity.

The line shape of the absorbance is determined by various broadening and shift mechanisms, including natural broadening, Doppler broadening and shift, resonance broadening, van der Waals broadening and shift, and Stark broadening and shift [19]. Natural broadening is usually three orders of magnitude smaller than the Doppler broadening and hence is neglected in the current study. Resonance broadening is also small and neglected because there is no allowed transition coupling the $O(3s\,^5S^o)$ and $O(3p\,^5P_3)$ states to the ground state. Doppler broadening is the most significant broadening mechanism for the 777- and 926-nm transitions within the current temperature range of 10 000 to 11 000 K, as shown in Fig. 2. In the current study, the Doppler full-width at half-maximum (FWHM) of the 777-nm absorbance is used to infer the translational temperature of the gas because of its better signal-to-noise ratio (SNR). For gas with a Maxwellian velocity distribution, the Doppler broadening line shape is a Gaussian function characterized by its FWHM, $\Delta\nu_D$. $\Delta\nu_D$ is given by [20]

$$\Delta\nu_D = \nu_0\left(\frac{8kT\ln 2}{mc^2}\right)^{\frac{1}{2}} = 7.16\times10^{-7}\nu_0\left(\frac{T}{M_O}\right)^{\frac{1}{2}}, \tag{3}$$

where k is the Boltzmann constant, m is the mass in kg, c is the speed of light, ν_0 is the transition line-center frequency in cm^{-1}, T is the translational temperature in K, and M_O is the molecular weight of atomic oxygen. For temperatures from 8 000 to 11 000K, $\Delta\nu_D$ ranges from 0.21 to 0.25 cm^{-1}. The Doppler shift is neglected because the gas behind the reflected shock is generally considered to be stagnant.

The Stark broadening and shift are caused by collisions between the absorber and other charged particles. The FWHM of Stark broadening (in Å) is given by [21–23]

$$\Delta\lambda_{\mathrm{Stark}} \approx 2\left[1 + 1.75\times10^{-4} n_e^{\frac{1}{4}}\alpha\left(1 - 0.068 n_e^{\frac{1}{6}} T_e^{-\frac{1}{2}}\right)\right] \times 10^{-16} w n_e \tag{4}$$

and the shift (in Å) is

$$\delta\lambda_{\mathrm{Stark}} \approx \left[\left(\frac{d}{w}\right) \pm 2.0\times10^{-4} n_e^{\frac{1}{4}}\alpha\left(1 - 0.068 n_e^{\frac{1}{6}} T_e^{-\frac{1}{2}}\right)\right] \times 10^{-16} w n_e, \tag{5}$$

where T_e is the electron translational temperature, n_e is the electron number density, w is the electron impact half-width, d/w is the relative electron-impact shift, and α is the ion-broadening parameter. The values of w, d, α for the atomic oxygen transitions in this study can be found in Griem's book [23]. The electron number density is inferred from the Stark shift of the 926-nm transition using Eq. (5). The large magnitude of the 926-nm Stark shift makes it sensitive to n_e and robust to noise.

The van der Waals broadening and shift are caused by the collisions of the absorber with charge neutral particles. Theoretical predictions of the van der Waals broadening and shift have large uncertainties in general.

The van der Waals broadening and the Stark broadening have Lorentzian line shapes, characterized by their FWHMs $\Delta\nu_{\mathrm{vdw}}$ and $\Delta\nu_s$. The total collisional broadening FWHM, $\Delta\nu_c$, is simply the summation of the two FWHMs.

Comparisons of Doppler broadening $\Delta\nu_d$, van der Waals broadening $\Delta\nu_{\mathrm{vdw}}$, and Stark broadening $\Delta\nu_s$ width at $P = 0.5$ atm are shown in Fig. 2 for the 777- and 926-nm transitions. The electron number density used to calculate $\Delta\nu_s$ in Fig. 2 is 2.5×10^{21} m^{-3}, which is the maximum electron number density at $T_{5,0} = 11\,200$ K inferred from the Stark shift of the 926-nm transition in the current experiment. It is of note that according to the current measurements and model predictions, the electron number density does not reach the

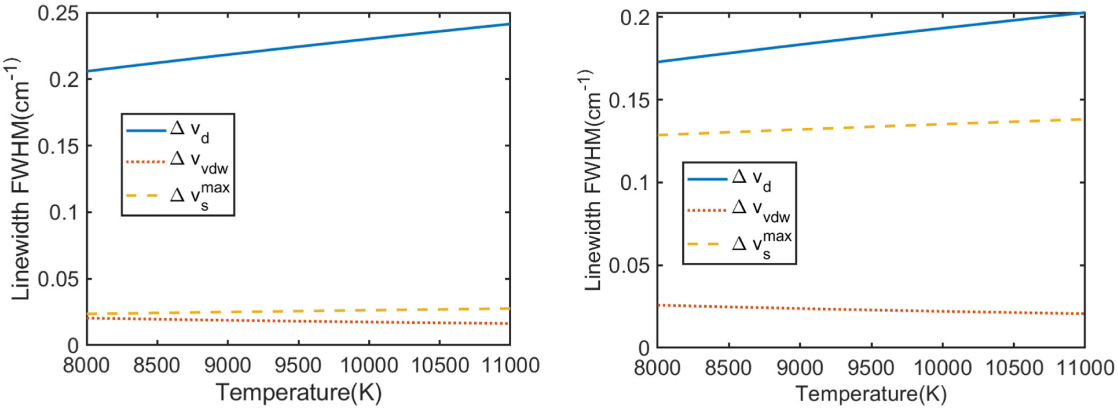

(a) (b)

FIG. 2. Comparison of Doppler broadening $\Delta\upsilon_d$, van der Waals broadening $\Delta\upsilon_{\text{vdw}}$, and Stark broadening $\Delta\upsilon_s^{\text{max}}$ at 0.5 atm for (a) the 777-nm transition and (b) the 926-nm transition. The Stark broadening $\Delta\upsilon_s^{\text{max}}$ is calculated using the maximum n_e of the measurements, $n_e = 2.5 \times 10^{21}$ m^{-3}.

value corresponding to chemical equilibrium and the translational temperature drops continuously due to Ar ionization within the test time (around 500 μs). The combined effect of these two makes the Stark broadening almost 10 times smaller than what is given by the Saha-Boltzmann formula at 11 200 K. Therefore, the Doppler-broadening width dominates the line shape of the 777-nm transition within the test time in all experiments of this study.

The spectral line shape of absorbance α_ν for the 777- and 926-nm transitions is fitted using a Voigt function, which is the convolution of Gaussian and Lorentzian line shapes. The MATLAB function `lsqcurvefit` is used to minimize the residual sum of squares of absorbance given by

$$e(\Delta\nu_d, \Delta\nu_c, A, \nu_0) = \sum_{\nu}(\alpha(\nu, \Delta\nu_d, \Delta\nu_c, A, \nu_0) - \alpha_m(\nu))^2, \tag{6}$$

where $\alpha_m(\nu)$ is the measured absorbance for each scan, $\alpha(\nu, \Delta\nu_d, \Delta\nu_c, A, \nu_0)$ is the fitted absorbance, $\Delta\nu_d$ and $\Delta\nu_c$ are the fitted Doppler and collisional broadening, A is the fitted integrated area of absorbance, and ν_0 is the fitted line-center frequency:

$$\Delta\nu_d{}^*, \Delta\nu_c{}^*, A^*, \nu_0^* = \arg \min_{\Delta\nu_d, \Delta\nu_c, A, \nu_0} e(\Delta\nu_d, \Delta\nu_c, A, \nu_0). \tag{7}$$

The Stark shift of each scan is determined by the relative line-center shift with respect to the first scan that has a reliable Voigt fit. The van der Waals broadening can be estimated from the collisional broadening of the first scan that has a reliable Voigt fit. The Stark broadening of each scan can be estimated by subtracting the van der Waals broadening from the overall collisional broadening.

C. Time-histories measurements

Number density n_4 and T_{tr} are inferred from the integrated area and Doppler broadening FWHM of the 777-nm absorbance. Number density n_6 and n_e are inferred from the integrated area and the Stark shift of the 926-nm absorbance. Sample measurements of the raw laser intensity and absorbance at 777 and 926 nm can be found in our previous work [18]. Because of the high energy gap and the strong chemical nonequilibrium of the O(3p $^5P_3$) state (relative to the ground state), the population of atomic oxygen in the O(3p $^5P_3$) state is typically low (on the order of 10^{15} m^{-3}). To maintain a sufficient signal-to-noise ratio (SNR) of the 926-nm transition, the experimental temperatures ($T_{5,0}$) of n_6 and n_e were limited to 10 000 K and above.

Sample measurements of the four time histories, n_4, n_6, n_e, and T_{tr} at $T_{5,0} = 10\,153$ K, $P_{5,0} = 0.5$ atm are shown in Fig. 3. Errors bars in this figure represent the 95% confidence intervals of the fitted and inferred values. Also shown in Fig. 3 are the simulation results of the optimized kinetic model, which are elaborated in detail in Sec. III B.

1. Time history of atomic oxygen population in the O(3s $^5S^o$) and **O(3*p* $^5P_3$)** *states*

Figures 3(a) and 3(b) show the population time histories of atomic oxygen in the O(3s $^5S^o$) and O(3p $^5P_3$) states, obtained from the integrated area of the absorbance using Eq. (1). The n_4 time history shows three stages, dominated by the heavy-particle-impact excitation, the electron impact de-excitation, and the electron impact excitation reactions, respectively, according to our model. The n_6 time history also shows multiple stages, but they are not as obvious as those of n_4. The fitting error bars are larger in the n_6 measurement than the n_4 measurement because of the smaller population of atomic oxygen in the energy level 6, and therefore worse SNR for the 926-nm transition data. The measured population time histories show that atomic oxygen in the levels 4 and 6 are not in chemical equilibrium with atomic oxygen in the ground state; i.e., both of them deviate from the calculations from the Boltzmann distribution.

In equilibrium, the ith energy level population for atomic oxygen follows a Boltzmann distribution given by

$$\frac{n_i^{\text{eq}}}{n_{\text{total}}} = \frac{g_i}{Q_O} \exp\left(-\frac{E_{i1}}{kT}\right), \tag{8}$$

where n_i^{eq} is the equilibrium population of the ith energy level, g_i is the degeneracy of the ith energy level, E_{i1} is the

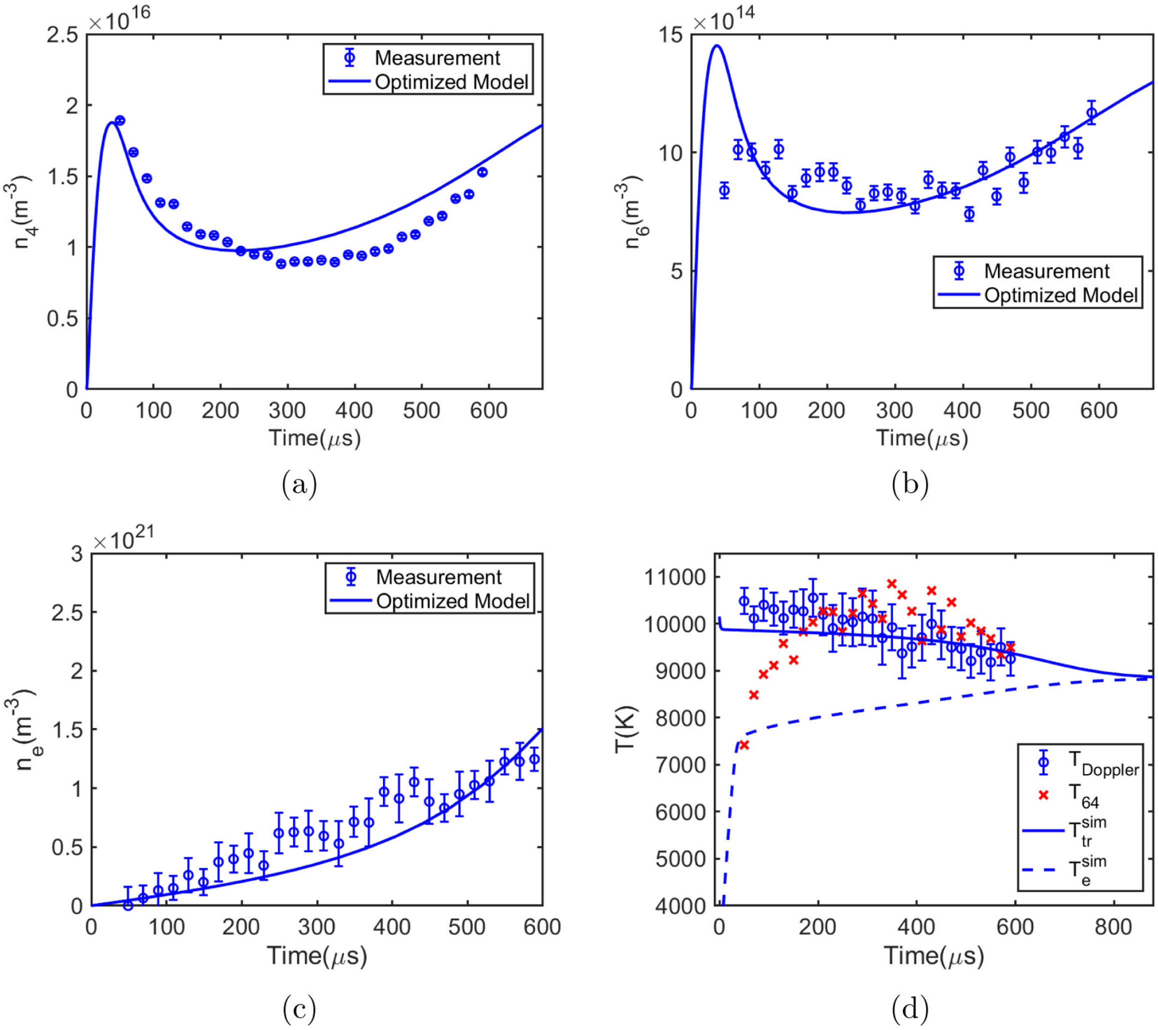

(a)

(b)

(c)

(d)

FIG. 3. Time-history measurements and model predictions of (a) population of O(3s ^{5}S^o), n_4; (b) population of O(3p $^5P_3$), n_6; (c) electron number density, n_e; (d) temperature, at $T_{5,0} = 10\,153$K, $P_{5,0} = 0.49$ atm. T_{Doppler} is inferred from 777-nm Doppler broadening; T_{64} is inferred from the ratio of measured populations in levels 4 and 6; and $T_{\text{tr}}^{\text{sim}}$, T_e^{sim} are model-predicted heavy-particle and electron translational temperature. Errors bars in this figure represent the 95% confidence interval of the fitted and inferred values from Voigt fits.

energy difference between the ith energy level and the ground state atomic oxygen (hence the subscript "1"), Q_O is the partition function of atomic oxygen, and T is the equilibrium temperature.

A nonequilibrium factor for the excited-state atomic oxygen is defined here to be its measured population normalized by its Boltzmann equilibrium population as calculated at the simulated translational temperature using Eq. (8). For example, the nonequilibrium factor for the fourth energy level is n_4/n_4^{eq}, where n_4 is the experimental measurement and n_4^{eq} is calculated using Eq. (8) at the simulated translational temperature.

The nonequilibrium factors for atomic oxygen in the O(3s $^5S^o$) and O(3p $^5P_3$) states are shown in Fig. 4. Figure 4(a) shows the population normalized by equilibrium value assuming the simulated heavy-particle translational temperature, T_{tr}, in Eq. (8). The O* population time histories are smaller than the equilibrium values assuming T_{tr}. The population of atomic oxygen in the O(3p $^5P_3$) state deviates more from its equilibrium value than the O(3s $^5S^o$) state, presumably due to its larger energy gap and lower excitation rates. After around 400 μs, the population of atomic oxygen in both states rise toward equilibrium (equivalently, nonequilibrium factors increase toward 1) because of the increase in electron translational temperature and electron number density. Figure 4(b) shows the population normalized by equilibrium value assuming the simulated electron translational temperature, T_e, in Eq. (8). The O* states are close to being in equilibrium with electrons at later test times and their nonequilibrium factors are close to 1. This is because at later test times there are sufficient electrons and T_e is large enough. The electrons dominate the collisional excitation of O*. The initial nonequilibrium factor is larger than 1 in Fig. 4(b) because of the low initial electron temperature (300 K) in the model.

2. *Electron number density time history*

Electron number density, n_e, is one of the most important quantities in the kinetic model because electrons are much more efficient in exciting the atomic species compared with

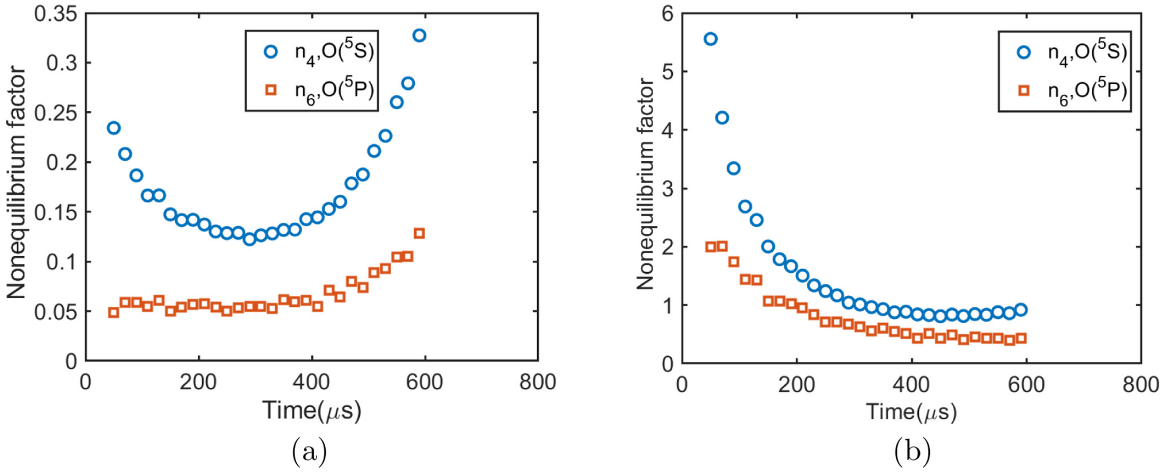

FIG. 4. Normalized population time-histories for O($3s\ ^5S^o$) and O($3p\ ^5P_3$) states at the same $T_{5,0}$, $P_{5,0}$ of Fig. 3. (a) Normalized at the simulated heavy-particle translational temperature. (b) Normalized at the simulated electron translational temperature. O* population is close to being in equilibrium with electrons at the later test time.

heavy particles. By utilizing the laser diagnostic technique recently developed in our group [18], electron number density is inferred from the 926-nm absorbance Stark shift; the corresponding n_e time history for $T_{\mathrm{tr},0} = 10\,153$ K in Ref. [18] is reproduced in Fig. 3(c).

The direct measurement of n_e time history in the current study verifies that electrons are produced at a rate much faster than the prediction considering only Ar ionization. This will be further elaborated in Sec. II B.

3. Temperature time history

Figure 3(d) shows the Doppler temperature, T_{Doppler}, inferred from 777-nm Doppler broadening FWHM using Eq. (8); the population temperature, T_{64}, calculated from the population ratio of levels 4 and 6 using Eq. (8); and the model-predicted (see Sec. III B) heavy-particle translational temperature, $T_{\mathrm{tr}}^{\mathrm{sim}}$, and the electron translational temperature, T_e^{sim}.

The measured Doppler temperature generally agrees with the simulated translational temperature within the ±5% fitting error bar. The simulated translational temperature first drops $\approx$ 300K from the initial $T_{5,0}$ of 10 153K due to the endothermic O_2 dissociation, then further drops $\approx$800K due to the endothermic Ar ionization within the test time. At the same time, the electron temperature increases continuously within the test time until reaching thermal equilibrium with the heavy-particle translational temperature at $\approx$8900 K beyond our test time.

The population temperature T_{64} is calculated from the population n_4, n_6 using

$$\frac{n_6}{n_4} = \frac{g_6}{g_4} \exp\left(-\frac{E_{64}}{kT_{64}}\right), \tag{9}$$

where g_4, g_6 are the degeneracy of atomic oxygen in the energy levels 4 and 6, and n_4, n_6 are the measured population of atomic oxygen in the energy levels 4 and 6.

The population temperature T_{64} is lower than the translational temperature in the first 100 μs because population of atomic oxygen in the level 4 increases more quickly than that at level 6 due to heavy-particle excitation rate constant k_{14} is larger than k_{16}. From around 100 μs to the end of the test time, T_{64} is approximately in agreement with the heavy-particle translational temperature [$T_{\mathrm{tr}}^{\mathrm{sim}}$ in Fig. 3(d)]. This indicates that the relative populations of atomic oxygen in the energy levels 4 and 6 are close to those calculated from the Boltzmann distribution at the corresponding translational temperature, although Fig. 4 shows that they are not individually in chemical equilibrium with the ground state. These results suggest that reaction X in Table II, the heavy-particle-impact collisional excitation/de-excitation, is very fast and in partial equilibrium, although the whole system is not in chemical equilibrium. These observations provide insight regarding tuning of the rate constant k_{46} in the kinetic model in Sec. III B.

D. Uncertainty analysis

The shock velocity error for the current study is 0.5%, which corresponds to a temperature uncertainty of about 1%. The pressure rise within the test time is mitigated by using a driver insert [24] to be below 5% within the test time for most cases. The rise time of the Kistler pressure transducer is less than 5 μs. Uncertainty of time zero for the experiment is less than 5μs.

The uncertainty analysis of the electron number density is discussed in Ref. [18]. Line-center shift uncertainties from the Voigt fit and the systematic experimental effects are on the order of 15%. The uncertainty in the Stark shift formula is hard to quantify without a detailed quantum mechanical calculation and other n_e diagnostics to validate. A discrepancy of 50% was reported previously between the measured and the predicted Stark shift for some atomic oxygen transitions [25].

The fitting uncertainties for n_4, n_6, and T_{tr} are on the order of 1%, 5%, and 5%, respectively. Considering other systematic experimental effects, the uncertainties for these quantities are estimated to be on the order of 5–10%.

TABLE II. Collisional and radiative processes included in the current model. The prefactors of the 12 atomic collisional excitation rate constants, $\exp(F_i)$, $i = 1, \ldots, 12$, are optimized to match the measured time histories of $n_4, n_6, n_e, T_{\mathrm{tr}}$ using the stochastic gradient descent algorithm and reported in Table III.

Label	Reaction	Forward rate constant formula	Reference
I	$\mathrm{Ar} + \mathrm{O_2} = \mathrm{Ar} + 2\mathrm{O}(g)$	$k_{dis} = 3.9 \times 10^{12}(T_{\mathrm{tr}})^{-1}\exp(-59380K/T_{\mathrm{tr}})\,\mathrm{m^3/mol\ s}$	[26]
II	$\mathrm{Ar} + \mathrm{O}(g) = \mathrm{Ar} + \mathrm{O}(^5S^0)$	$k_{14} = \exp(F_1) \times 2\sqrt{\frac{2}{\pi m_{Ar,O}}}\beta_{14}(kT_{\mathrm{tr}})^{1/2}(E_{41} + 2kT_{\mathrm{tr}})\exp\left(-\frac{E_{41}}{kT_{\mathrm{tr}}}\right)\mathrm{m^3/s}$	[17]
III	$e^- + \mathrm{O}(g) = e^- + \mathrm{O}(^5S^0)$	$k^e_{14} = \exp(F_2) \times 8.629 \times 10^{-6}/g_1/T_e^{1/2}\gamma_{14}\exp\left(-\frac{E_{41}}{kT_e}\right)\mathrm{m^3/s}$	[27]
IV	$\mathrm{Ar} + \mathrm{Ar} = \mathrm{Ar} + \mathrm{Ar}^+ + e^-$	$k^M_{Ar,c} = \exp(F_3) \times 1.68 \times 10^{-26}T_{\mathrm{tr}}^{1.5}\left(\frac{\theta_{A*,1}}{T_{\mathrm{tr}}} + 2\right)\exp\left(-\frac{\theta_{A*,1}}{T_{\mathrm{tr}}}\right)\mathrm{m^3/s}$	[28,29]
V	$e^- + \mathrm{Ar} = e^- + \mathrm{Ar}^+ + e^-$	$k^e_{Ar,c} = \exp(F_4) \times 3.75 \times 10^{-22}T_e^{1.5}\left(\frac{\theta_{A*,1}}{T_e} + 2\right)\exp(-\frac{\theta_{A*,1}}{T_e})\,\mathrm{m^3/s}$	[28,29]
VI	$\mathrm{Ar} + \mathrm{O}(^5S^0) = \mathrm{Ar} + e^- + \mathrm{O}^+$	$k^M_{4c} = \exp(F_5) \times 64\pi a_0^2\left(\frac{E^H}{E_{4c}}\right)^2\left(\frac{kT_{\mathrm{tr}}}{\pi m_{Ar}}\right)^{\frac{1}{2}}\zeta^2\frac{m_e m_{Ar}}{m_H(m_e+m_{Ar})}\psi(w_{4c})\ \mathrm{m^3/s}$	[30]
VII	$e^- + \mathrm{O}(^5S^0) = e^- + e^- + \mathrm{O}^+$	$k^e_{4c} = \exp(F_6) \times 4\pi a_0^2\left(\frac{8kT_e}{\pi m_e}\right)^{\frac{1}{2}}\alpha\left(\frac{E_{4c}}{kT_e}\right)^2 I_2(a_{4c})\ \mathrm{m^3/s}$	[1]
VIII	$\mathrm{Ar} + \mathrm{O}(g) = \mathrm{Ar}\ + \mathrm{O}(3p^5P_3)$	$k_{16} = \exp(F_7) \times 2\sqrt{\frac{2}{\pi m_{Ar,O}}}\beta_{16}(kT_{\mathrm{tr}})^{1/2}(E_{61} + 2kT_{\mathrm{tr}})\exp\left(-\frac{E_{61}}{kT_{\mathrm{tr}}}\right)\mathrm{m^3/s}$	[17]
IX	$e^- + \mathrm{O}(g) = e^- + \mathrm{O}(3p^5P_3)$	$k^e_{16} = \exp(F_8) \times 8.629 \times 10^{-6}/g_1/T_e^{1/2}\gamma_{16}\exp\left(-\frac{E_{61}}{kT_e}\right)\mathrm{m^3/s}$	[27]
X	$\mathrm{Ar} + \mathrm{O}(3p^5P_3) = \mathrm{Ar} + e^- + \mathrm{O}^+$	$k^M_{6c} = \exp(F_9) \times 64\pi a_0^2\left(\frac{E^H}{E_{6c}}\right)^2\left(\frac{kT_{\mathrm{tr}}}{\pi m_{Ar}}\right)^{\frac{1}{2}}\zeta^2\frac{m_e m_{Ar}}{m_H(m_e+m_{Ar})}\psi(w_{6c})\ \mathrm{m^3/s}$	[30]
XI	$e^- + \mathrm{O}(3p^5P_3) = e^- + e^- + \mathrm{O}^+$	$k^e_{6c} = \exp(F_{10}) \times 4\pi a_0^2\left(\frac{8kT_e}{\pi m_e}\right)^{\frac{1}{2}}\alpha\left(\frac{E_{6c}}{kT_e}\right)^2 I_2(a_{6c})\ \mathrm{m^3/s}$	[1]
XII	$\mathrm{Ar} + \mathrm{O}(^5S^0) = \mathrm{Ar} + \mathrm{O}(3p^5P_3)$	$k_{46} = \exp(F_{11}) \times 2\sqrt{\frac{2}{\pi m_{Ar,O}}}\beta_{46}(kT_{\mathrm{tr}})^{1/2}(E_{64} + 2kT_{\mathrm{tr}})\exp\left(-\frac{E_{64}}{kT_{\mathrm{tr}}}\right)\mathrm{m^3/s}$	[17]
XIII	$e^- + \mathrm{O}(^5S^0) = e^- + \mathrm{O}(3p^5P_3)$	$k^e_{46} = \exp(F_{12}) \times 8.629 \times 10^{-6}/g_4/T_e^{1/2}\gamma_{46}\exp\left(-\frac{E_{64}}{kT_e}\right)\mathrm{m^3/s}$	[27]
XIV	$\mathrm{O}(^5S^0) \rightarrow \mathrm{O}(g) + \mathrm{h}\nu$	$A_{41} = 5.56 \times 10^3\mathrm{s^{-1}}$	[31]
IV	$\mathrm{O}(3p^5P_3) \rightarrow \mathrm{O}(^5S^0) + \mathrm{h}\nu$	$A_{64} = 3.69 \times 10^7\mathrm{s^{-1}}$	[1,31]

III. MODELING RESULTS

A. The two-temperature collisional-radiative (CR) model

1. Collisional and radiative processes

The current study extends a previous collisional-radiative model [17] to include atomic oxygen in the $\mathrm{O}(3p\ ^5P_3)$ state and seven more reactions involving atomic oxygen in this state. As shown in table II, 15 collisional and radiative processes are included in the current model: $\mathrm{O_2}$ dissociation, electron/heavy-particle impact excitation of atomic oxygen to $\mathrm{O}(3s\ ^5S^o)$ and $\mathrm{O}(3p\ ^5P_3)$ states, electron/heavy-particle collisions between atomic oxygen in the $\mathrm{O}(3s\ ^5S^o)$ and $\mathrm{O}(3p\ ^5P_3)$ states, electron/heavy-particle impact ionization of atomic oxygen in the $\mathrm{O}(3s\ ^5S^o)$ and $\mathrm{O}(3p\ ^5P_3)$ states, electron/heavy-particle impact ionization of Ar, spontaneous emission of atomic oxygen in the $\mathrm{O}(3s\ ^5S^o)$ and $\mathrm{O}(3p\ ^5P_3)$ states. The formulas for reaction rate constants are adapted from the literature and presented in table II, and the calculated rate constants from the literature are referred to as the "nominal values" and used as the initial guesses for the optimization procedure described in Algorithm 1. Each nominal rate constant for the atomic collision is multiplied by a prefactor $\exp(F_i)$, $i = 1, \ldots, 12$ in table II to match the measured time histories. In Sec. III B, Algorithm 1 is used to optimize the logarithm of these prefactors, i.e., F_i.

Figure. 5 shows the energy diagram and 14 collisional and radiative processes of atomic oxygen. We follow the same notation as in Ref. [17] and use subscripts 1, 4, and 6 in the formulas for reaction rate constants to denote the ground state, $\mathrm{O}(g)$, and the excited $\mathrm{O}(3s\ ^5S^o)$ and $\mathrm{O}(3p\ ^5P_3)$ states of atomic oxygen, respectively. The superscript "e" denotes the reaction rate constants for electron impact reactions. Detailed discussions for most of the rate formulas can be found in a previous work [17]. The additional reaction rate constants involving atomic oxygen level 6 are discussed below.

The rate constant of heavy-particle excitation of atomic oxygen to the $\mathrm{O}(3p\ ^5P_3)$ state, i.e., k_{16}, is assumed to have the same form as k_{14} (the excitation reaction rate constant to $\mathrm{O}(3s\ ^5S^o)$ state) [17,32], with the exception that the activation energy is the energy gap between the $\mathrm{O}(3p\ ^5P_3)$ state and the ground state. Similarly, the cross-coupling rate between levels 4 and 6, k_{46}, is assumed to have the same form with k_{14} with the exception of using the energy gap between energy levels 4 and 6 as the activation energy. The cross-sectional slope constant, β_{46}, β_{16} are set to be equal to β_{14} in the nominal values in table II. It is of note that the cross-sectional slope constant is likely to be negatively correlated to the energy gap [33] and some of the nominal values in table II adapted from the empirical rate constant formulas, which are also used as initial guesses in the optimization procedure (Algorithm 1), may be far away from the optimized value, as suggested by the large values of some optimized prefactors shown in table III. For instance, the cross-sectional slope constant, β_{46}, is likely to be larger than the cross-sectional slope constant of β_{14} because the energy gap between levels 4 and 6 is smaller and the transition from level 4 to 6 is spin allowed while that from level 1 to 4 is spin forbidden. Correspondingly, the prefactor of k_{46} is optimized to be 6200 as shown in table III, indicating

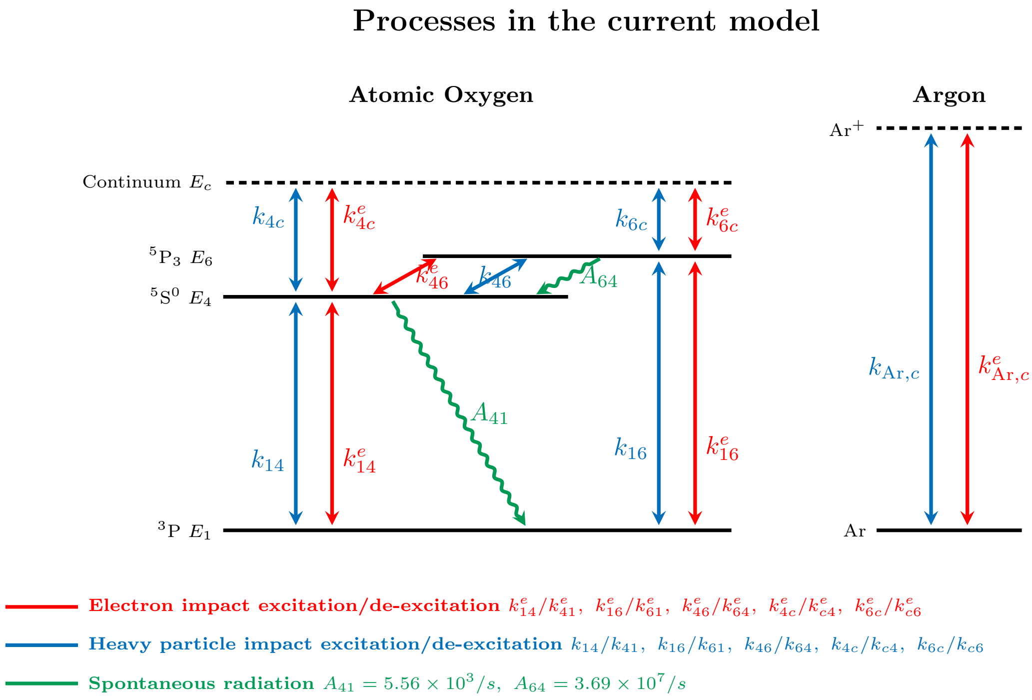

FIG. 5. Twelve collisional rate constants and two spontaneous emission rates in the current model. Two-way arrows indicate the collisional excitation and de-excitation reactions. One-way arrows indicate spontaneous emission. Blue, red, and green lines represent heavy-particle impact collisions, electron impact collisions, and spontaneous emission.

the initial guess of k_{46} is underestimated, probably due to $\beta_{46}/\beta_{14} \gg 1$. It will be further elaborated in Sec. III B 1.

The rate constant of electron impact excitation from ground state to O($3p\ ^5P_3$) state, k^e_{16}, is assumed to take the same form as that of the electron impact excitation reaction from ground state to O($3s\ ^5S^o$) [17,32], with the effective collision strength $\gamma_{16} = 1.76 \times 10^{-1}$ [27]. γ_{46} is set to be equal to the nominal values of γ_{14} as shown in Table II.

2. *Species and energy conservation equations*

The temporal variation in species number density is governed by a set of ordinary differential equations (ODE) similar to that in Ref. [17]. The reaction rate constants involving atomic oxygen in the O($3p\ ^5P_3$) state are included in the ODE. For example, the species conservation equation for atomic oxygen in the O($3p\ ^5P_3$) state is given by

$$\begin{aligned}\frac{\partial n_6}{\partial t} = \dot{n}_6 = {} & \big(k_{16} n_{\mathrm{O}(g)} n_{\mathrm{Ar}} + k^e_{16} n_e n_{O(g)} + k_{46} n_{\mathrm{O}(^5S^0)} n_{\mathrm{Ar}} \\ & + k^e_{46} n_e n_{\mathrm{O}(^5S^0)} + k^e_{c6} n_{\mathrm{O}^+} n_e^2 + k^M_{c6} n_{\mathrm{O}^+} n_e n_{\mathrm{Ar}}\big) \\ & - \big(k_{61} n_6 n_{\mathrm{Ar}} + k^e_{61} n_6 n_e + k_{64} n_6 n_{\mathrm{Ar}} + k^e_{64} n_6 n_e \\ & + k^e_{6c} n_e n_6 + k^M_{6c} n_6 n_{\mathrm{Ar}}\big) - \Lambda_{64} A_{64} n_6,\end{aligned} \tag{10}$$

TABLE III. Random initialization and optimized values of rate constant prefactors. Optimized prefactors are chosen with the minimal cost in multiple runs of SGD algorithm as described in Algorithm 1.

Rate constant	Reaction	Range of prefactors initial guess	Optimized prefactors
k_{14}	$\mathrm{Ar} + \mathrm{O}(g) = \mathrm{Ar} + \mathrm{O}(^5S^0)$	[exp(−1), exp(1)]	0.5
k^e_{14}	$e^- + \mathrm{O}(g) = e^- + \mathrm{O}(^5S^0)$	[exp(−1), exp(1)]	0.3
$k^M_{Ar,c}$	$\mathrm{Ar} + \mathrm{Ar} = \mathrm{Ar} + \mathrm{Ar}^+ + e^-$	[exp(2.5), exp(4.5)]	24
$k^e_{Ar,c}$	$e^- + \mathrm{Ar} = e^- + \mathrm{Ar}^+ + e^-$	[exp(2.5), exp(4.5)]	25
k^M_{4c}	$\mathrm{Ar} + \mathrm{O}(^5S^0) = \mathrm{Ar} + e^- + \mathrm{O}^+$	[exp(−1), exp(1)]	0.6
k^e_{4c}	$e^- + \mathrm{O}(^5S^0) = e^- + e^- + \mathrm{O}^+$	[exp(−1), exp(1)]	2.5
k_{16}	$\mathrm{Ar} + \mathrm{O}(g) = \mathrm{Ar} + \mathrm{O}(3p^5P_3)$	[exp(−1), exp(1)]	0.4
k^e_{16}	$e^- + \mathrm{O}(g) = e^- + \mathrm{O}(3p^5P_3)$	[exp(−1), exp(1)]	0.4
k^M_{6c}	$\mathrm{Ar} + \mathrm{O}(3p^5P_3) = \mathrm{Ar} + e^- + \mathrm{O}^+$	[exp(−1), exp(1)]	0.3
k^e_{6c}	$e^- + \mathrm{O}(3p^5P_3) = e^- + e^- + \mathrm{O}^+$	[exp(−1), exp(1)]	3.7
k_{46}	$\mathrm{Ar} + \mathrm{O}(^5S^0) = \mathrm{Ar} + \mathrm{O}(3p^5P_3)$	[exp(2.5), exp(4.5)]	6200
k^e_{46}	$e^- + \mathrm{O}(^5S^0) = e^- + \mathrm{O}(3p^5P_3)$	[exp(−1), exp(1)]	0.4

where the source term $\dot{n}_6$ is the volumetric production rate of atomic oxygen in the energy level 6. All the rate constants are listed in Table II. The escape factor [34], Λ_{64}, is negatively correlated to the absorption coefficient of the transition from energy level 4 to 6. In general, $\Lambda_{64} \approx 1$ for a small absorption coefficient and $\Lambda_{64} \approx 0$ for large absorption coefficient ($k \gg 1$). We assess the transition from energy level 6 to 4 to be optically thin, i.e., with small absorption coefficient, because the molar fraction of atomic oxygen in the energy level 4 is generally below 1 ppm in the current study. The escape factor is set to be 1 in the current model for simplicity. One might expect a stronger depletion of atomic oxygen in the energy level 6 than that at level 4 due to the four orders of magnitude larger spontaneous emission rate of A_{64} compared with A_{41} as shown in Table II. However, the current measurement results in Secs. II C 1 and II C 3 show that atomic oxygen in the levels 4 and 6 approximately follow the Boltzmann distribution at the translational temperature, indicating a large heavy-particle-impact cross-coupling rate between levels 4 and 6.

The electron and heavy-particle translational temperatures are used in the rate constant formulas that involve electrons and only heavy particles, respectively. The two temperatures are solved from the energy conservation equations similar to those in Ref. [17], but including the energy source terms due to reactions involving atomic oxygen of the O($3p\ ^5P_3$) state.

The energy conservation equation for electron is given by Panesi [1], Hoffert [28], and Kapper [35]:

$$\begin{aligned} n_e \frac{3}{2} k \frac{\partial T_e}{\partial t} &= \left[\frac{\partial E_e}{\partial t}\right]_{\text{Ion}} + \left[\frac{\partial E_e}{\partial t}\right]_{\text{Exc}} + \left[\frac{\partial E_e}{\partial t}\right]_{\text{Coll}} + \left[\frac{\partial E_e}{\partial t}\right]_{\text{Brem}} \\ &= -\dot{n}^e_{\text{Ar},c} E_{\text{Ar},c} - \dot{n}^e_{4c}(E_{\text{O},c} - E_{41}) - \dot{n}^e_{6c}(E_{\text{O},c} - E_{61}) - \dot{n}^e_{14} E_{41} - \dot{n}^e_{16} E_{61} \\ &\quad - \frac{2m_{Ae}}{m_e + m_A} \frac{3}{2} (\nu_{Ae} + \nu_{A^+e}) n_e k (T_e - T_{\text{tr}}) - 1.42 \times 10^{-40} Z_{\text{eff}}^2 T_e^{1/2} n_+ n_e. \end{aligned} \tag{11}$$

The five terms in the first line of Eq. (11) represent the loss of electron sensible energy due to electron impact Ar and O ionization, electron impact excitation of O atoms, Ar-electron and Ar$^+$-electron collisions, and Bremsstrahlung emission; $\dot{n}^e_{\text{Ar},c}$, $\dot{n}^e_{4c}$, $\dot{n}^e_{6c}$ are the electron impact ionization rates of Ar, atomic oxygen in the O($3s\ ^5S^o$) and O($3p\ ^5P_3$) states; $E_{\text{Ar},c}$ and $E_{\text{O},c}$ are the ionization energy of Ar and O atom; $\dot{n}_i$ is the volumetric reaction rate for producing species i [17]. The collision frequencies of Ar-electron and Ar$^+$-electron, i.e., ν_{Ae} and ν_{A^+e}, are given in Ref. [17]; $Z_{\text{eff}} = 1.67$ [35].

The heavy-particle energy conservation equation is given by [17]

$$\begin{aligned} \left(\sum_{i\in\Pi} n_i \frac{3}{2} k + n_{\text{O}_2} c_{v,\text{O}_2}\right) \frac{\partial T_{\text{tr}}}{\partial t} &= -\sum_{i\in\Pi} \dot{n}_i \left(\frac{3}{2} k T_{\text{tr}} + E_{\text{chem},i}\right) - \dot{n}_{\text{O}_2}(E_{\text{sens},O_2} + E_{\text{chem},O_2}) - \dot{n}_e \left(\frac{3}{2} k T_e + E_{\text{chem},e}\right) \\ &\quad + \dot{n}^e_{\text{Ar}^+} E_{\text{Ar},c} + \dot{n}^e_{4c}(E_{\text{O},c} + E_{41}) + \dot{n}^e_{6c}(E_{\text{O},c} - E_{41}) + \dot{n}^e_{14} E_{41} + \dot{n}^e_{16} E_{61} \\ &\quad + \frac{2m_{Ae}}{m_e + m_A} \frac{3}{2} (\nu_{Ae} + \nu_{A^+e}) n_e k (T_e - T_{\text{tr}}) - A_{41} E_{41} n_{\text{O}(^5S^0)} - A_{64} E_{64} n_{\text{O}(^5P_3)} \end{aligned} \tag{12}$$

where Π includes atomic oxygen in the O(g), O($^5S^o$), and O($^5P_3$) states, Ar, Ar$^+$, and O$^+$. $\dot{n}_i$ is the volumetric reaction rate for producing species i [17]. The chemical energy for the atomic species i, $E_{\text{chem},i}$, and for molecular oxygen, $E_{\text{chem},\text{O}_2}$, are taken from Ref. [36]. The sensible energy for O$_2$, $E_{\text{sens},\text{O}_2} = n_{\text{O}_2}(H_{\text{sens},\text{O}_2} - kT_{\text{tr}})$, where $H_{\text{sens},\text{O}_2}$ is the enthalpy per molecule calculated using the NASA Glenn coefficients [36].

B. Optimization of the CR model

1. *Optimization procedure using SGD algorithm of the 12 rate constant prefactors*

Twelve logarithmic prefactors of the collisional reaction rate constants in Table II, i.e., F_i, $i = 1, \ldots, 12$, are optimized by minimizing the cost function defined by Eq. (13) using the stochastic gradient descent (SGD), as described in Algorithm 1.

$$\begin{aligned} \text{Cost}(F_1, \ldots, F_{12}) &= \left(\frac{n_4^{\text{meas}} - n_4^{\text{sim}}}{||n_4^{\text{meas}}||_2}\right)^2 + \left(\frac{n_6^{\text{meas}} - n_6^{\text{sim}}}{||n_6^{\text{meas}}||_2}\right)^2 \\ &\quad + \left(\frac{n_e^{\text{meas}} - n_e^{\text{sim}}}{||n_e^{\text{meas}}||_2}\right)^2 + \left(\frac{T_{\text{tr}}^{\text{meas}} - T_{\text{tr}}^{\text{sim}}}{||T_{\text{tr}}^{\text{meas}}||_2}\right)^2, \end{aligned} \tag{13}$$

where $F_1, \ldots, F_{12}$ are the logarithm of the rate-constant prefactors in Table II; n_4^{meas}, n_6^{meas}, n_e^{meas}, $T_{\text{tr}}^{\text{meas}}$ are the measured time histories for the population of the atomic oxygen in the O($3s\ ^5S^o$), O($3p\ ^5P_3$) states, the electron number density, and the translational temperature; the superscript "sim" denotes the simulation results from the model. Normalization by the 2-norm of the measured time-history vectors accounts for the difference in magnitude of the residuals from the four different quantities.

For each shock in each epoch of the SGD procedure Algorithm 1, the logarithm of prefactors, i.e., $F_i (i = 1, \ldots, 12)$ are updated one time using the gradient of the cost function. The benefits of optimizing the logarithm of prefactors are twofold. First, since the reaction rate constants span multiple orders of magnitude, taking logarithms improves numerical stability. Second, by updating the prefactors on a log scale, i.e., updating F_i, we avoid dealing with the constraints that all reaction rate constants must be positive as $\exp(F_i)$ is always

Algorithm 1: Optimization procedure for the logarithm of prefactors in Tables II and III, F^*, using stochastic gradient descent algorithm.

```
Result: Optimized $F^*$ for the logarithm of the pre-factor for the twelve reaction
        rate constants in Table II and Table III
for each run of stochastic gradient descent do
    Initialization: random initialize the twelve pre-factors using the initial guess
      given in Table III;
    for $epoch = 1 : epoch_{max}$ do
        for each experiment do
            1. calculate reaction rate constants from current pre-factors
            2. evaluate cost for the current model using Equation 13
            3. evaluate gradient numerically $g' = \nabla_F \mathrm{Cost}$
            4. update $F$ by $F = F - \frac{\alpha}{N_t} g'$, where $\alpha$ is the learning rate and $N_t$ is the number of
               data points for one measured time-history.
        end
    end
end
pick the best set of optimized parameters corresponding to the smallest cost and set
  $F^*$ correspondingly.
```

positive. The gradient of the cost function with respect to each logarithmic prefactor F_i is numerically evaluated using Eq. (13) by perturbing F_i by a small fraction (e.g., $\delta = 1\%$), i.e., gradient

$$g_i' = \frac{\mathrm{Cost}(F_i + \delta F_i; F_j, \forall j \neq i) - \mathrm{Cost}(F_i - \delta F_i; F_j, \forall j \neq i)}{2\delta F_i}. \tag{14}$$

The algorithm generally converges to a local optimum after 50 epochs.

The SGD algorithm is run multiple times (e.g., five times in the current work) as described in Algorithm 1, each time with a set of random initialization of rate-constant prefactors given by Table III. The random initialization for most F_i are uniformly distributed within [−1,1]; therefore, the initial guesses for prefactors are $\sim \exp(U(-1, 1))$ where $U(-1, 1)$ is the uniform distribution between -1 to 1. The optimized prefactor values for these rate constants are generally on the order of 1 as shown in Table III. The set of rate-constant prefactors corresponding to the minimum cost among the five runs are reported as the "optimized prefactors" in Table III.

Three prefactors in Table III are initialized with $\sim \exp(U(2.5, 4.5))$, namely, the rate constants $k_{\mathrm{Ar},c}$, $k^e_{\mathrm{Ar},c}$, and k_{46}. The large initial guesses for the prefactors of the two Ar ionization rate constants are chosen to improve the speed of converge. The faster electron number density production rate in the measurement yields prefactors for $k_{\mathrm{Ar},c}$, $k^e_{\mathrm{Ar},c}$ on the order of 24 and 25, i.e., 24 and 25 times larger than the nominal values reported by Kelly's measurements [29]. The large discrepancy between the current inferred rates and the well-established rate constants is likely due to the simplifications in the model to neglect critical oxygen ionization processes and/or ionization of impurities in the shock tube.

Besides the two Ar ionization rates, the prefactor of the cross-coupling rate constant between levels 4 and 6, k_{46}, is also uniformly randomly initialized to be within $\exp(U(2.5, 4))$ as shown in Table III. A large prefactor of k_{46} is expected for the following three reasons. First, large collisional excitation rate constants are needed to compensate the large spontaneous emission rate A_{64}. Figure 6 illustrates this effect. It shows the time-history measurements normalized by the maximum measurement values, as well as the normalized model-predicted time histories using the nomi-

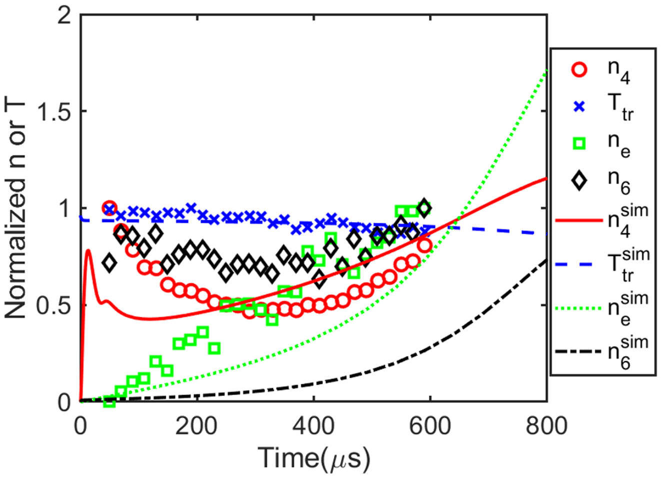

FIG. 6. Normalized time histories at the same $T_{5,0}$, $P_{5,0}$ of Fig. 3. Circles: time-history measurements normalized by their maximum. Lines: normalized model predictions using nominal rate constants in Table II, i.e., prefactors of $\exp(F_i)$ are set to 1 ($F_i = 0$).

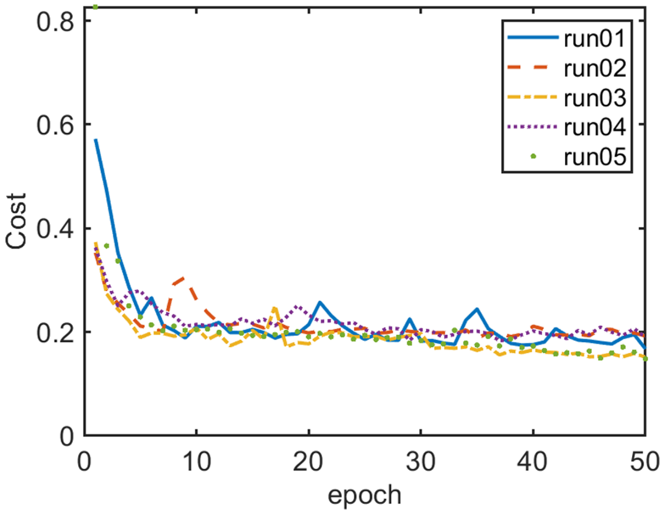

FIG. 7. Trajectory of the cost function against epoch number (one epoch is one pass through all experimental data) using SGD algorithm. The set of rates with the minimum cost are reported in Table III. Each run has a different set of random initialization as described in Table III.

nal rate constant values in Table II; i.e., pre-factors F_is are set to be 1. It is of note that the nominal rate constants adapted from the previous model were developed by matching only the time-history measurements of atomic oxygen in the O($3s\ ^5S^o$) state and applicable over 8 000–10 000 K [17]. Small discrepancies between the current measurement of n_4 and the simulation with the nominal rate constants could be due to the extension of the temperature range. The large discrepancy between the simulated and the measured n_6 within the test time is caused by the large spontaneous emission rate (i.e., large A_{64} in Table II), which dominates the n_6 time history over the other collisional excitation reactions (correspondingly, k_{16}, k^e_{16}, k_{46}, k^e_{46}) in the model. This discrepancy indicates that the collisional excitation rate constants are larger than their nominal values. The population temperature T_{64} in Fig. 3(d) is close to the heavy-particle translational temperature instead of the electron temperature, indicating the heavy-particle cross-coupling reactions between atomic oxygen levels 4 and 6 are in partial equilibrium, i.e., large k_{46}. Second, the theoretical prediction of k_{46} is not as well established as other rate constants involving ground-state atomic oxygen and electrons and likely to be under-estimated as explained in Sec. III A 1. Third, atomic oxygen in the other excited states besides levels 1, 4, and 6 (such as levels 5, 3, and 2 and other states not included in the current kinetic model) could also contribute to the collisional excitation of atomic oxygen in the level 6. Such effects are also incorporated into the prefactor of k_{46} in the current study.

2. Optimization results of 12 rate constant prefactors

Figure 7 shows the cost versus the epoch number of the SGD algorithm for five different initializations of the rate constant prefactors. An epoch is defined as one training pass through all experimental data. The algorithm generally converges after 10 epochs and costs from all five runs are close after 50 epochs of training.

Table III shows the "optimized" rate constants prefactors, which gives the minimum cost at the last epoch among the five runs. The majority of these rate-constant prefactors are on the order of 1. The heavy-particle and electron impact Ar ionization rate constants are optimized to be 24 and 25 times larger than their nominal values measured by Kelly *et al.* [29], which presumably are caused by the model simplification which neglects critical oxygen ionization and systematic experimental effects such as ionization from impurities, as explained before.

The current optimized value of heavy-particle collisional transfer rate constant k_{46}, although multiplied by a seemingly large prefactor of 6200, is consistent with Dagdigian's previous measurements [37] of the collisional transfer rate from atomic oxygen in the level 7 [O($3p\ ^3P$)] to level 6 [O($3p\ ^5P$)]. Dagdigian *et al.* [37] measured this rate constant by collisions with O_2, N_2 to be $k_{76}(O_2) = 6\times10^{-17}$, $k_{76}(N_2) = 2\times10^{-17}\ m^3/s$ at room temperature. Considering that the Ar-O collisional excitation is likely to be less efficient compared with O_2-O collisional excitation but the current temperatures are approximately 37 times higher than room temperature, the current optimized value of heavy-particle cross-coupling rate constant of $k_{64}(Ar) = 6.7\times10^{-17}\ m^3/s$ at 11209 K seems consistent with Dagdigian's measurements. It is of note that the hard-sphere collisional rate constant is $1.3\times10^{-15}\ m^3/s$ at 11 209K for Ar-O collisions.

Figure 8 shows the updates to individual rate constant logarithmic prefactors by the SGD algorithm. Figure 8(a) shows the trajectory of 12 logarithmic prefactors versus epoch number. The largest three rate-constant logarithmic prefactors, i.e., k_{46}, $k_{\mathrm{Ar},c}$, $k^e_{\mathrm{Ar},c}$, converge within 10 epochs. Figure 8(b) shows the updates to the logarithmic prefactor of k_{46} against epoch number for five SGD runs with different random initialization. In all five runs, the logarithmic prefactor of k_{46} converges to approximately the same value after 10 epochs. It is of note that not all logarithmic prefactors converge to the same values

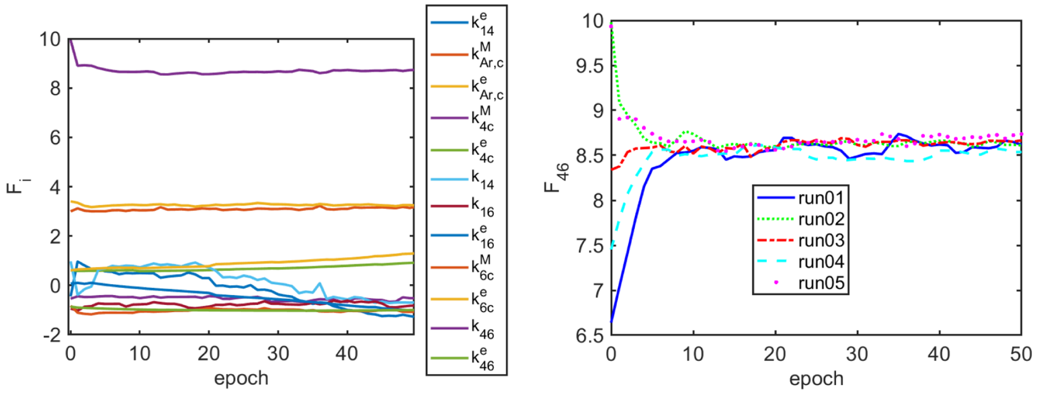

(a) (b)

FIG. 8. (a) Updates of the 12 rate-constant logarithmic prefactors against epoch number for the run of SGD with the minimum cost. The top three lines show prefactors for rate constants k_{46}, $k^e_{\mathrm{Ar},c}$, $k^M_{\mathrm{Ar},c}$ are much larger than 1. Other prefactors are on the order of 1. (b) Updates of k_{46} logarithmic prefactor for five different SGD runs.

for different initialization, especially for those with very small sensitivity coefficients as defined in the next section. The current algorithm provides a method to determine a set of rate constants that can be used to model atomic oxygen collisional-excitation kinetics given the measured time histories.

Figure 9 shows the comparison between the measurements and the simulations (using optimized rate constants) for the time histories of n_4, n_6, n_e, T_{tr} normalized by their maximum measured values over $T_{5,0}$ from 10 100 to 11 200 K. The model predictions show reasonably good agreement with the data

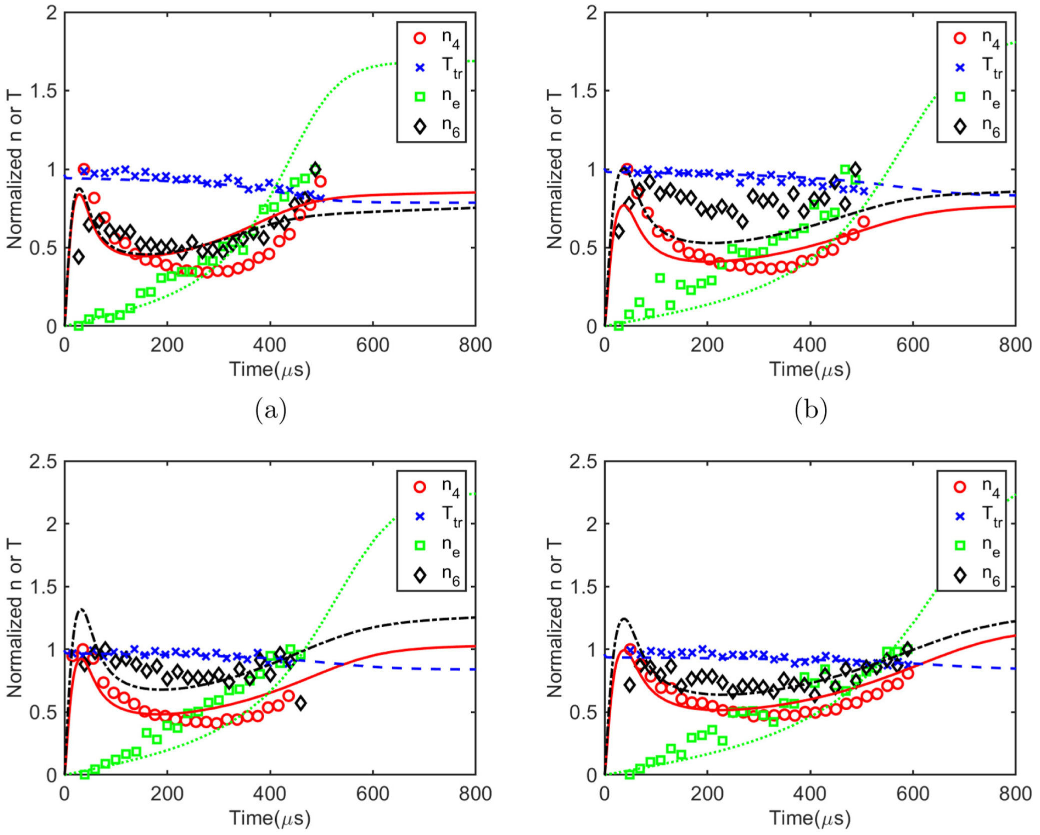

(a) (b) (c) (d)

FIG. 9. Time-history measurements (symbols) and simulations (lines) with the optimized rate constants in Table III for n_4, n_6, n_e, T_{tr} normalized by their maximum measured values. (a) $T_{5,0} = 11\,209$ K, $P_{5,0} = 0.37$ atm, (b) $T_{5,0} = 10\,923$ K, $P_{5,0} = 0.33$ atm, (c) $T_{5,0} = 10\,623$ K, $P_{5,0} = 0.44$ atm, and (d) $T_{5,0} = 10\,153$ K, $P_{5,0} = 0.49$ atm. The line style has the same meaning as in Fig. 6.

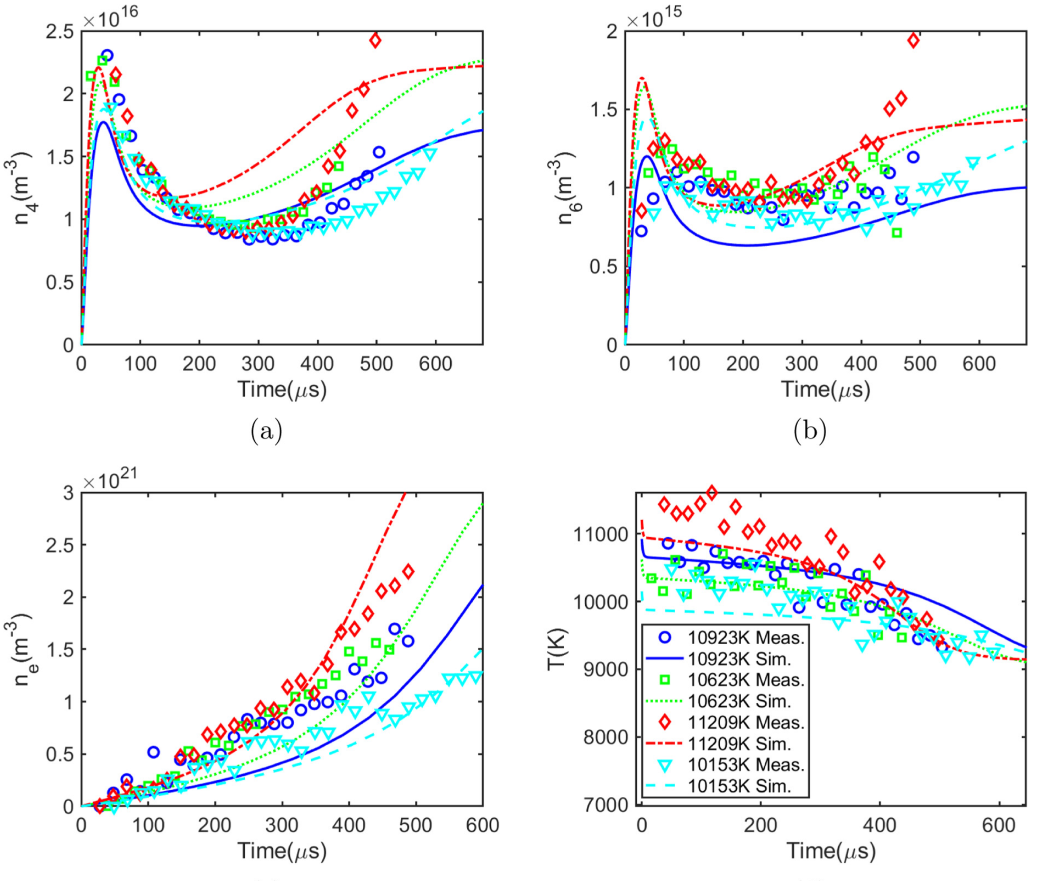

(a) (b)

(c) (d)

FIG. 10. Absolute values of (a) n_4, (b) n_6, (c) n_e, and (d) temperature from 10 100–11 200 K. Symbols: measurements. Lines: simulations using optimized models with rate constants in Table III.

in most cases. The model predictions of n_4 after 200 μs, n_6 for the first 100 μs, and T_{tr} for the first 200 μs have larger discrepancies with the data. The absolute values of the time histories for the n_4, n_6, n_e, and T_{tr} are reported in Fig. 10 for use by others seeking to model our data.

3. Sensitivity analysis

Sensitivity analysis of the 12 optimized collisional rate constants are performed for n_4, n_6, n_4, T_{tr} time histories. The sensitivity coefficient of the jth rate constant, k_j, for the time history of A, denoted as $[A]$, is calculated by perturbing the corresponding rate constants by a factor of 2 in both positive and negative directions,

$$S_j = \frac{[A]_{2k_j}(t) - [A]_{k_j/2}(t)}{[A]_{k_j}(t)} \frac{k_j}{2k_j - 0.5k_j}, \qquad (15)$$

where $[A]_{2k_j}(t)$ and $[A]_{k_j/2}(t)$ are the time-history simulation of $[A]$ with rate constant k_j multiplied by 2 and 1/2.

Figure 11(c) shows that for electron number density n_e, the most sensitive reaction rate constants are $k^M_{Ar,c}$, $k^e_{Ar,c}$. This is because Ar ionization is the main pathway for electron production in the current model. Figure 11(d) shows that the translational temperature T_{tr} is insensitive to almost all the rates within the test time. This is because the translational temperature changed only a small fraction (<10%) due to Ar ionization and oxygen dissociation within the test time. Figure 11(a) shows that for n_4, the most sensitive reactions are k_{14}, k^e_{14}, $k^M_{\mathrm{Ar},c}$, $k^e_{\mathrm{Ar},c}$, k^M_{4c}, k_{16}. Figure 11(b) shows that for n_6, the most sensitive reactions include all the above sensitive reactions for n_4, plus k_{46}. The large sensitivity of k_{46} is corroborated by the large optimized logarithmic prefactor of k_{46} (i.e., 6200 as shown in Table III).

IV. CONCLUSION

In this paper, we studied the collisional excitation kinetics for atomic oxygen, using the n_4, n_6, n_e, and T_{tr} time histories inferred from the absorbance of two atomic oxygen transitions at 777 and 926 nm. The electron number density measurements verify the faster electron production rates as hypothesized in our previous paper [17]. The n_4 and n_6 measurements show that the atomic oxygen in the energy levels 4 and 6, i.e., the O($3s\ {}^5S^o$) and O($3p\ {}^5P_3$) states, are in chemical nonequilibrium with atomic oxygen in the ground state, but achieve a partial equilibrium with each other within the test time of approximately 500 μs. Translational temperature inferred from the Doppler linewidth drops within the test time because of oxygen dissociation and Ar ionization. The four measured time histories are utilized to optimize the collisional-excitation rate constants of the sim-

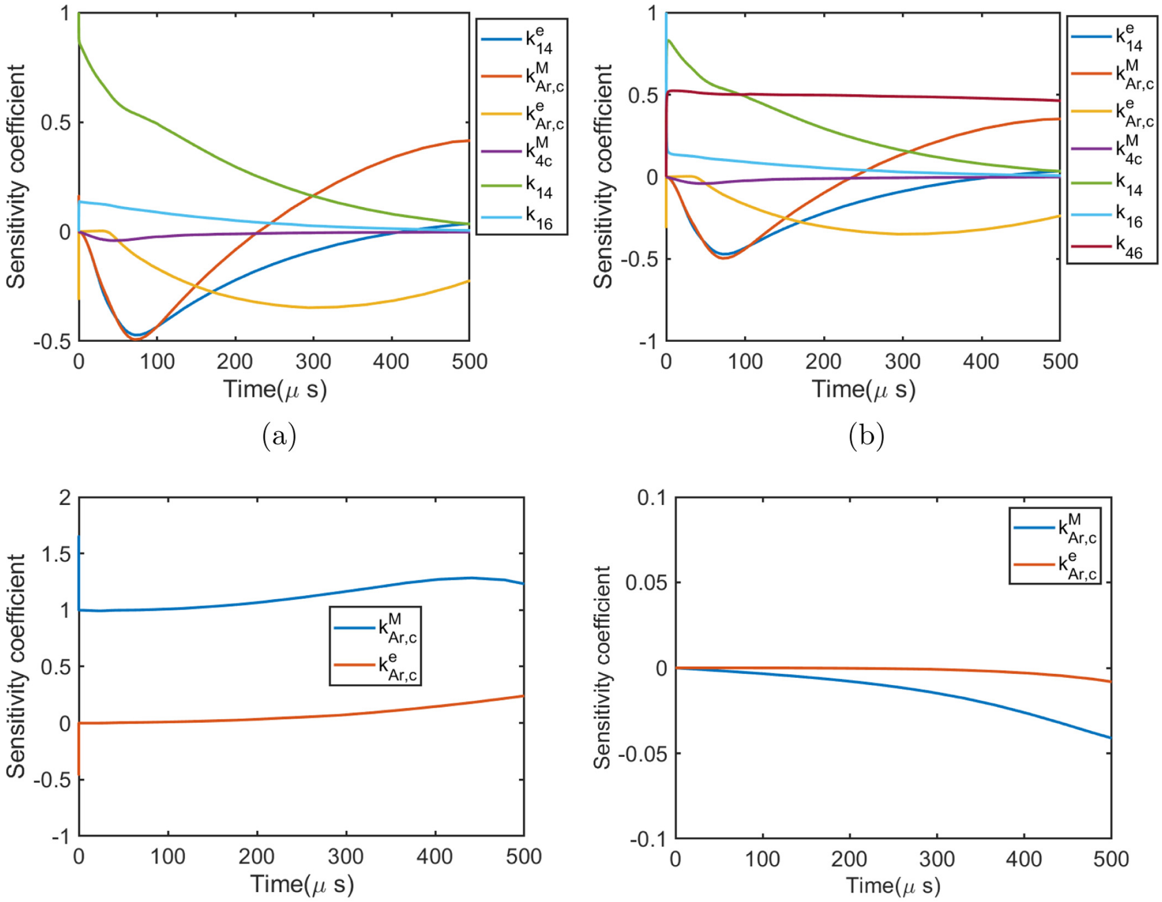

(a) (b) (c) (d)

FIG. 11. Sensitivity coefficients of the most sensitive reactions for n_4, n_6, n_e, T_{tr} time histories. Only a few of the largest sensitive rate constants are shown.

plified two-temperature collisional-radiative model using the SGD algorithm. The heavy-particle collisional cross-coupling rate constant between atomic oxygen in the energy levels 4 and 6, k_{46}, is found to be 6200 times larger than the nominal value adapted from the literature, to compete with the large spontaneous emission rate of A_{64} and maintain partial equilibrium between atomic oxygen in the energy levels 4 and 6. The current time-history data, diagnostic methods, and collisional-radiative model may prove useful in other studies of high-enthalpy air, plasma processing or other applications involving weakly ionized oxygen, e.g., re-entry flow modeling, and the data reported here may be useful to other researchers seeking to assemble kinetic models of O-atom excitation and ionization.

ACKNOWLEDGMENTS

The authors thank Mark A. Cappelli, Christopher L. Strand, Shengkai Wang, Leo Hollberg, David Miller, and Jay B. Jeffries for helpful discussions. The authors also thank a reviewer for offering an interesting interpretation of the data. This work was supported by the Air Force Office of Scientific Research (AFOSR) under Grant No. FA9550-16-1-0291.

---

[1] M. Panesi, T. E. Magin, and A. Bourdon, Fire II flight experiment analysis by means of a collisional-radiative model, J. Thermophys. Heat Transfer **23**, 236 (2009).

[2] A. Bultel, B. G. Chéron, A. Bourdon, O. Motapon, and I. F. Schneider, Collisional-radiative model in air for earth re-entry problems, Phys. Plasmas **13**, 43502 (2006).

[3] X. Y. Wang, C. Yan, Y. K. Zheng, and E. L. Li, Assessment of chemical kinetic models on hypersonic flow heat transfer, Int. J. Heat Mass Transf. **111**, 356 (2017).

[4] A. Bultel and J. Annaloro, Elaboration of collisional-radiative models for flows related to planetary entries into the Earth and Mars atmospheres, Plasma Sources Sci. Technol. **22**, 025008 (2013).

[5] D. Olynick, W. D. Henline, L. Chambers, and G. V. Candler, Comparison of coupled radiative flow solutions with project fire II flight data, J. Thermophys. Heat Trans. **9**, 586 (1995).

[6] G. V. Candler and R. W. MacCormack, Computation of weakly ionized hypersonic flows in thermochemical nonequilibrium, J. Thermophys. Heat Trans. **5**, 266 (1991).

[7] C. Park, Review of chemical-kinetic problems of future NASA missions, I: Earth entries, J. Thermophys. Heat Trans. **7**, 385 (1993).

[8] A. Lemal, C. M. Jacobs, M. Y. Perrin, C. O. Laux, P. Tran, and E. Raynaud, Air collisional-radiative modeling with heavy-particle impact excitation processes, J. Thermophys. Heat Trans. **30**, 226 (2014).

[9] C. Park, *Nonequilibrium Hypersonic Aerothermodynamics* (Wiley-Interscience, New York, 1990).

[10] C. O. Laux, Optical diagnostics and radiative emission of air plasmas, Ph.D. thesis, Stanford University, Stanford, CA, 1999.

[11] T. G. Owano, Nonequilibrium behavior in a flowing, atmospheric pressure plasma, Ph.D. thesis, Stanford University, Stanford, CA, 1991.

[12] C. O. Johnston, B. R. Hollis, and K. Sutton, Non-Boltzmann modeling for air shock-layer radiation at lunar-return conditions, J. Spacecr. Rockets **45**, 879 (2008).

[13] F. Bonelli, M. Tuttafesta, G. Colonna, L. Cutrone, and G. Pascazio, An MPI-CUDA approach for hypersonic flows with detailed state-to-state air kinetics using a GPU cluster, Comput. Phys. Commun. **219**, 178 (2017).

[14] G. Colonna, F. Bonelli, and G. Pascazio, Impact of fundamental molecular kinetics on macroscopic properties of high-enthalpy flows: The case of hypersonic atmospheric entry, Phys. Rev. Fluids **4**, 033404 (2019).

[15] M. Nations, S. K. Wang, C. S. Goldenstein, D. F. Davidson, and R. K. Hanson, Kinetics of excited oxygen formation in shock-heated O_2-Ar mixtures, J. Phys. Chem. A **120**, 8234 (2016).

[16] S. M. Jo, O. J. Kwon, and J. G. Kim, Electronic-state-resolved analysis of high-enthalpy air plasma flows, Phys. Rev. E **100**, 033203 (2019).

[17] Y. Li, S. K. Wang, C. L. Strand, and R. K. Hanson, Two-temperature collisional-radiative modeling of partially ionized O_2-Ar mixtures over 8000–10 000 K behind reflected shock waves, J. Phys. Chem. A **124**, 3687 (2020).

[18] Y. Li, S. K. Wang, C. Strand, and R. K. Hanson, Development of a Stark shift measurement technique using excited state oxygen atoms to determine electron number density in shock heated O2/Ar above 10 000 K, Plasma Sources Sci. Technol. **30**, 025007 (2021).

[19] C. Laux, T. G. Spence, C. H. Kruger, and R. N. Zare, Optical diagnostics of atmospheric pressure air plasmas. Plasma Sources Science and Technology **12**, 125 (2003).

[20] R. Hanson, R. Spearrin, and C. Goldenstein, *Spectroscopy and Optical Diagnostics for Gases* (Springer International, Geneva, Switzerland, 2016).

[21] W. L. Wiese, in *Plasma Diagnostic Techniques*, edited by R. Huddlestone and L. Stanley (Academic Press, New York, 1965).

[22] D. S. Baer, H. A. Chang, and R. K. Hanson, Fluorescence diagnostics for atmospheric-pressure plasmas using semiconductor lasers, J. Opt. Soc. Am. B **9**, 1968 (1992).

[23] H. Griem, *Spectral Line Broadening by Plasmas* (Elsevier, Amsterdam, 2012).

[24] Z. K. Hong, G. A. Pang, S. S. Vasu, D. F. Davidson, and R. K. Hanson, The use of driver inserts to reduce non-ideal pressure variations behind reflected shock waves, Shock Waves **19**, 113 (2009).

[25] A. Goly and S. Weniger, Widths and shifts of some plasma-broadened oxygen and carbon multiplets, J. Quant. Spectrosc. Radiat. Transfer **38**, 225 (1987).

[26] J. W. Streicher, A. Krish, R. K. Hanson, K. M. Hanquist, R. S. Chaudhry, and I. D. Boyd, Shock-tube measurements of coupled vibration-dissociation time histories and rate parameters in oxygen and argon mixtures from 5000 K to 10 000 K, Phys. Fluids **32**, 076103 (2020).

[27] O. Zatsarinny and S. S. Tayal, Electron collisional excitation rates for OI using the *B*-spline *R*-matrix approach, Astron. Astrophys. Suppl. Ser. **148**, 575 (2003).

[28] M. I. Hoffert and H. Lien, Quasi-one-dimensional, nonequilibrium gas dynamics of partially ionized two-temperature argon, Cit. Phys. Fluids **10**, 1769 (1967).

[29] A. J. Kelly, Atom-atom Ionization cross sections of the noble gases—argon, krypton, and xenon, J. Chem. Phys. **45**, 1723 (1966).

[30] H. W. Drawin and F. Emard, Atom-atom excitation and ionization in shock waves of the noble gases, Phys. Lett. A **43**, 333 (1973).

[31] A. Kramida, Y. Ralchenko, J. Reader, and the NIST ASD Team, NIST Atomic Spectra Database (ver. 5.6.1), http://physics.nist.gov/.

[32] J. Vlcek, A collisional-radiative model applicable to argon discharges over a wide range of conditions. I. Formulation and basic data, J. Phys. D: Appl. Phys. **22**, 623 (1989).

[33] A. Bultel, B. Van Ootegem, A. Bourdon, and P. Vervisch, Influence of Ar_2^+ in an argon collisional-radiative model, Phys. Rev. E **65**, 046406 (2002).

[34] T. Holstein, Imprisonment of resonance radiation in gases. II, Phys. Rev. **83**, 1159 (1951).

[35] M. G. Kapper and J. L. Cambier, Ionizing shocks in argon. Part I: Collisional-radiative model and steady-state structure, J. Appl. Phys. **109**, 113308 (2011).

[36] B. J. McBride, M. J. Zehe, and S. Gordon, National Aeronautics and Space Administration, John H. Glenn Research Center at Lewis Field Report No. TP-2002-211556, 2002.

[37] P. J. Dagdigian, B. E. Forch, and A. W. Miziolek, Collisional transfer between and quenching of the $3p$ $3P$ and $5P$ states of the oxygen atom, Chem. Phys. Lett. **148**, 299 (1988).